Metal Matrix–Metal Nanoparticle Composites with Tunable Melting Temperature and High Thermal Conductivity for Phase-Change Thermal Storage

Minglu Liu,[†] Yuanyu Ma,[‡] Hsinwei Wu,[‡] and Robert Y. Wang*[,†,‡]

[†]Department of Mechanical Engineering and [‡]Department of Material Science & Engineering, Arizona State University, Tempe, Arizona 85287, United States

ABSTRACT Phase-change materials (PCMs) are of broad interest for thermal storage and management applications. For energy-dense storage with fast thermal charging/discharging rates, a PCM should have a suitable melting temperature, large enthalpy of fusion, and high thermal conductivity. To simultaneously accomplish these traits, we custom design nanocomposites consisting of phase-change Bi nanoparticles embedded in an Ag matrix. We precisely control nanoparticle size, shape, and volume fraction in the composite by separating the nanoparticle synthesis and nanocomposite formation steps. We demonstrate a 50–100% thermal energy density improvement relative to common organic PCMs with equivalent volume fraction. We also tune the melting temperature from 236–252 °C by varying nanoparticle diameter from 8.1–14.9 nm. Importantly, the silver matrix successfully prevents nanoparticle coalescence, and no melting changes are observed during 100 melt–freeze cycles. The nanocomposite's Ag matrix also leads to very high thermal conductivities. For example, the thermal conductivity of a composite with a 10% volume fraction of 13 nm Bi nanoparticles is 128 ± 23 W/m-K, which is several orders of magnitude higher than typical thermal storage materials. We complement these measurements with calculations using a modified effective medium approximation for nanoscale thermal transport. These calculations predict that the thermal conductivity of composites with 13 nm Bi nanoparticles varies from 142 to 47 W/m-K as the nanoparticle volume fraction changes from 10 to 35%. Larger nanoparticle diameters and/or smaller nanoparticle volume fractions lead to larger thermal conductivities.

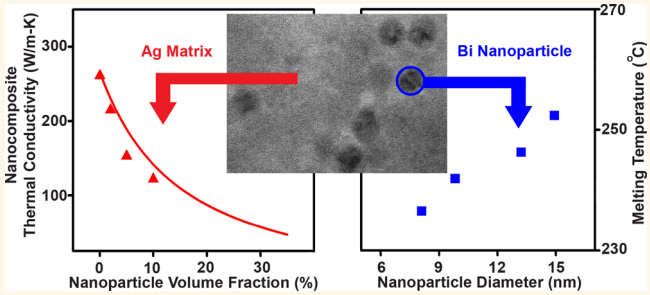

KEYWORDS: metal nanocomposites · solution-phase synthesis · tunable melting temperature · high thermal conductivity · phase-change material · size-dependent melting

Latent heat thermal storage systems utilize the solid–liquid transition of phase-change materials (PCMs) to store thermal energy. This results in much higher energy densities than commonly used sensible heat thermal storage systems and in turn leads to both material and space savings.[1−3] For instance, the latent heat of ice is equivalent to 80 degrees Celsius of sensible heat in water. Nevertheless, challenges exist for employing PCMs for effective latent heat thermal storage in varying environmental conditions. Commercially used PCMs are mostly organics and salt hydrates, which are limited to applications from 10 to 120 °C.[4] This is suitable for thermal management of buildings[5] and typical electronics[6] but is mismatched for higher temperature applications such as industrial process heat,[7] power electronics thermal management,[8] and concentrated solar thermal power plants.[9] Latent heat storage at elevated temperatures has been generally restricted to phase-change salts in laboratory settings,[10] whereas industrial practice instead focuses on molten salts for sensible heat storage.[9,11] However, salts are prone to corrosion problems and also suffer from low thermal conductivity, which in turn leads to slow thermal charging/discharging rates. In fact, this issue of low thermal conductivity is common to thermal storage

* Address correspondence to rywang@asu.edu.

Received for review September 19, 2014 and accepted January 22, 2015.

Published online January 22, 2015
10.1021/nn505328j

materials in general.[12−14] The thermal conductivities of organic PCMs and salt hydrates range from ∼0.1−1 W/m-K,[4] and the thermal conductivity of salts range from ∼0.5−5 W/m-K.[10]

Previous efforts to improve the thermal conductivity of PCMs have focused on the use of thermally conductive filler materials (*e.g.*, graphite,[15] metallic nanoparticles,[16] and carbon nanotubes[17]) or foams (*e.g.*, metal[18] and graphite[19]). While fillers are easy to implement, thermal conductivity enhancements are unfortunately limited because the fillers do not form a continuous structure and the thermal interface resistance between the PCM and fillers is non-negligible. To overcome this problem, many researchers infiltrate PCM into thermally conductive foams (*i.e.*, metal foam[18] and graphite foam[19]), which have a continuous structure and lead to better thermal conductivity improvements. For example, a recent study using a graphite foam−paraffin wax composite demonstrated a thermal conductivity of 3.6 W/m-K, which is an 18-fold improvement over paraffin.[12] The use of foams has been demonstrated for many low melting temperature organic PCMs; however, this technique is problematic for high melting temperature PCMs (*e.g.*, salt) due to difficulties with the infiltration process and corrosivity.[20]

To find a PCM that has high thermal conductivity, high melting temperature, and large enthalpy of fusion, we turned our focus to metallic materials. Metals have excellent thermal conductivities ranging from ∼10 to 400 W/m-K and a broad range of melting temperatures ranging from −40 to over 3000 °C. Relative to other PCMs, metals have received little attention primarily due to their weight (*i.e.*, poor gravimetric energy density).[1,14] While gravimetric energy density is important for mobile applications, many thermal storage applications are stationary, and in these cases volumetric energy density is of more importance. Hence, metallic PCMs could find applications in buildings thermal management, industrial process heat, and concentrated solar thermal power plants.

In this paper, we propose the use of composites that consist of phase-change metallic inclusions distributed in a metal matrix. The phase-change inclusions provide the desired melting temperature and high volumetric energy density, whereas the matrix provides excellent thermal transport and mechanical strength when the inclusions melt. Furthermore, we explore the use of phase-change nanoparticle inclusions as opposed to phase-change macroparticle inclusions. The choice of nanoparticles is motivated by the use of size-dependent melting as a new PCM design tool. Size-dependent melting is a commonly observed phenomenon in nanostructures and was first predicted by Pawlow.[21] Substantial theoretical and experimental efforts have since been devoted to explaining the relationship between nanoparticle diameter and melting temperature.[22−28] These fundamental studies inspired us to develop nanoparticle-based PCMs for application purposes.

We demonstrate this nanoparticle-based PCM concept by creating composites consisting of phase change Bi nanoparticles embedded in an Ag matrix. We first present a solution-phase approach to embed high-quality colloidal Bi nanoparticles into a bulk Ag matrix. This approach separates the nanoparticle synthesis and composite formation steps, thereby enabling excellent control over nanoparticle morphology and volume fraction. This in turn permits control over the composite's melting temperature and energy density. We investigate the composite's thermal storage performance by using cyclic differential scanning calorimetry (DSC). Our composite's energy density is 50−100% better than composites containing an equivalent volume fraction of typical organic PCMs. Furthermore, varying the Bi nanoparticle diameter tunes the nanocomposite's melting temperature from 236 to 252 °C. Importantly, these DSC measurements also demonstrate that the silver matrix offers effective protection against coalescence of the Bi nanoparticles during melt−freeze cycles. The Ag matrix also greatly improves thermal transport in the nanocomposite. Thermal conductivity measurements using the Wiedemann−Franz law[29] demonstrate that our nanocomposite's thermal conductivity is several orders of magnitude better than typical thermal storage materials. We also employ a modified effective medium approximation (EMA) for nanoscale thermal transport to calculate the composite thermal conductivity over a broad range of nanoparticle diameters and volume fractions.

RESULTS AND DISCUSSION

Metal Matrix−Metal Nanoparticle Composite Synthesis. The nanocomposite was prepared by a simple three-step approach: (a) synthesis of colloidal Bi nanoparticles, (b) codissolution of Bi nanoparticles and Ag precursor in a solvent mixture, and (c) heating to thermally decompose the Ag precursor into an Ag matrix. This three-step nanocomposite approach enables independent control of nanoparticle size, shape, and volume fraction by using a modular technique that separates nanoparticle synthesis from nanocomposite formation. Nanoparticle size and shape are controlled by step (a), whereas nanoparticle volume fraction is controlled by step (b). The formation of the metal matrix−metal nanoparticle composite occurs in the last step, during which the Ag precursor thermally decomposes into an Ag matrix that encapsulates the Bi nanoparticles.

The Bi nanoparticles were prepared by a hot injection technique reported by Yarema *et al.*[30] In brief, $Bi[N(SiMe_3)_2]_3$ was used as a Bi precursor and reduced by hexadecylamine at an elevated temperature.

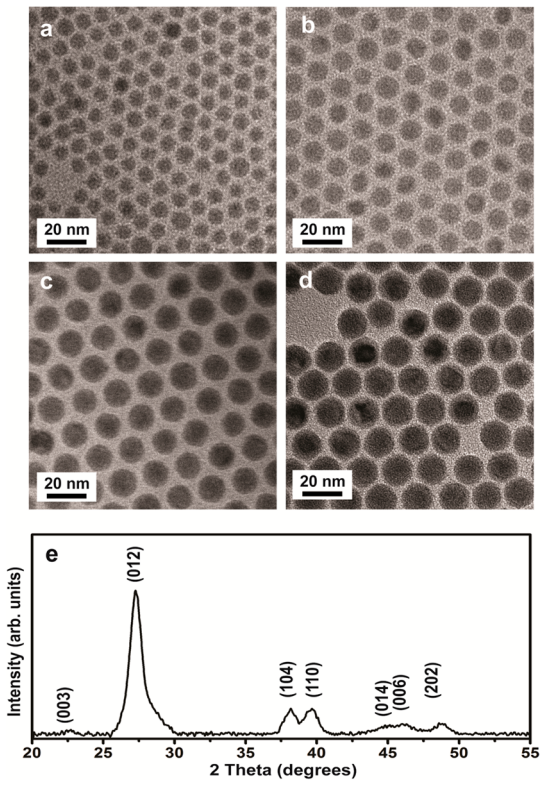

Figure 1. Transmission electron microscopy images of the Bi nanoparticles used to create the Ag matrix–Bi nanoparticle composites. The nanoparticle diameters are (a) 8.1 ± 1.0, (b) 9.8 ± 0.8, (c) 13.2 ± 0.6, and (d) 14.9 ± 0.6 nm. (e) X-ray diffraction pattern of Bi nanoparticles with 13.6 nm diameter.

Size variation was achieved by varying the reaction temperature from 115 to 140 °C. This synthesis yields Bi nanoparticles with surface-bound hexadecylamine ligands. In order to improve colloidal nanoparticle stability, the hexadecylamine ligands were exchanged with oleic acid ligands postsynthesis. Figure 1 illustrates the high-quality Bi nanoparticles prepared by this approach, which exhibit spherical shape, excellent size control, and narrow size distribution.

We used silver benzoate as the precursor to create the nanocomposite's Ag matrix. Silver benzoate is an organic silver salt with good solubility in amine solvents and is a well-known silver precursor.[31,32] Thermogravimetric analysis was employed to identify appropriate conditions for decomposing this precursor. A temperature ramp of 2 °C/min was performed from room temperature to 300 °C, where the sample was kept isothermal for 2 h, and then resumed up to 350 °C. As Figure 2a shows, after the isotherm process at 300 °C, the mass reached its final value of ~47% and no further decrease in mass was observed. This mass ratio indicates that the final product is Ag, and this conclusion is further corroborated by X-ray diffraction measurements (Figure 2b). Together, these results indicate that 300 °C is sufficient to fully decompose the silver benzoate.

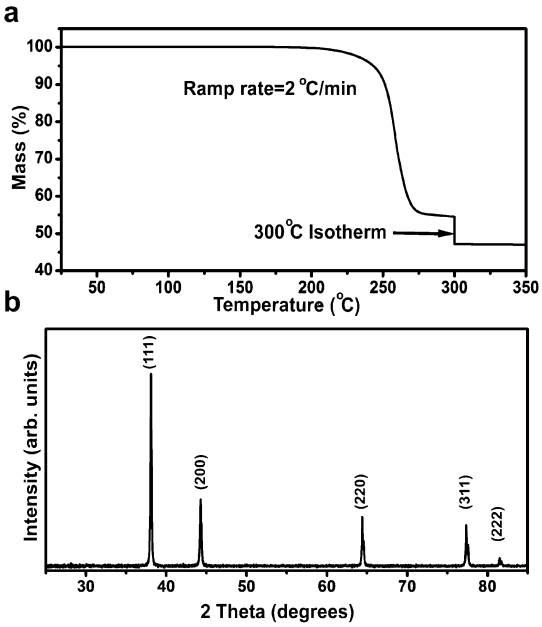

Figure 2. (a) Thermogravimetric analysis on silver benzoate. The temperature ramp rate was 2 °C/min, and a 2 h isotherm was applied at 300 °C. (b) X-ray diffraction pattern of silver made *via* the thermal decomposition of silver benzoate.

Prior to nanocomposite formation, the Bi nanoparticles and silver benzoate were mixed in an appropriate ratio to yield the desired nanoparticle volume fraction. We note that this step is sensitive to solvent choice because the Bi nanoparticles prefer nonpolar solvents whereas the silver benzoate prefers mildly polar solvents. We addressed this issue by choosing a miscible solvent pair and controlling the concentration of Bi nanoparticles and silver benzoate. Prior to mixing, the Bi nanoparticles were suspended in toluene at ~1 mg/mL and the silver benzoate was dissolved in pyridine at ~2 mg/mL. The Bi nanoparticle suspension and silver benzoate solution were then combined, stirred for 2 h, and used promptly. If not used promptly, partial precipitation could be observed the following day. We also chose toluene and pyridine as the miscible solvent pair because of their similar boiling temperatures, which should help prevent phase segregation as the solvent evaporates during the nanocomposite formation step. We note that since pyridine is a known ligand for colloidial nanocrystals,[33,34] a potential for ligand exchange between oleic acid and pyridine exists during this step. However, we do not believe ligand exchange occurs because the Bi nanoparticles with oleic acid ligands are insoluble in pyridine. Had a ligand exchange occurred, the Bi nanoparticles should be soluble in pyridine and our use of a pyridine–toluene solvent pair would be unnecessary.

Composites used for phase-change studies were prepared by drop-casting the combined Bi nanoparticle–silver benzoate solution, solvent removal at 100 °C, and then silver benzoate thermal decomposition at 300 °C for

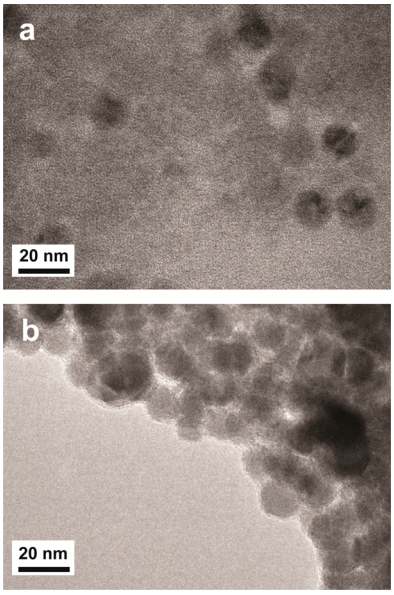

Figure 3. (a) TEM image of a Bi−Ag nanocomposite with a low Bi nanoparticle volume fraction. (b) TEM image of a Bi−Ag nanocomposite with a high Bi nanoparticle volume fraction.

2 h. The results of this nanocomposite formation process are shown in Figure 3. The size and shape preservation of the Bi nanoparticles during this process is most clearly seen in Figure 3a, which has a low Bi volume fraction. Figure 3b shows a composite with a large volume fraction of Bi nanoparticles, which is more representative of the composites used for phase-change studies (*i.e.*, Figures 4 and 5). To confirm the homogeneous dispersion of the Bi nanoparticles throughout the matrix, we imaged a composite over a large area and collected chemical composition maps using energy-dispersive X-ray spectroscopy (Figure S1, Supporting Information). Nanocomposite pores, which arise due to silver benzoate's mass loss during thermal decomposition, are also visible in Figure S1 (Supporting Information).

Despite the decomposition temperature of the silver benzoate being above the melting temperature of the Bi, we do not observe any alloying between the Bi nanoparticles and Ag matrix. This is primarily because the phase behavior of Ag−Bi is such that no compounds form between these elements.[35] In addition, the solubility of Ag in Bi is negligibly small and the solubility of Bi in Ag is only 0.83% at 262 °C.[35] We also believe the oleic acid ligands protect the Bi nanoparticles during silver benzoate decomposition. In our past work on Bi nanoparticle melting inside polymer matrices,[35] Bi nanoparticle melting was only observed after an initial "break-in" period at elevated temperature (*e.g.*, 1 h at 300 °C). We presume this is due to the oleic acid ligands stabilizing the Bi surface and temporarily inhibiting melting. Similar surface stabilization effects have been observed in other literature such as Pb nanoparticles in Al matrices[36] and Ag nanoparticles in Ni matrices.[37]

Unlike typical *in situ* metal nanocomposite formation techniques (*i.e.*, ball milling,[38,39] melt spinning,[40,41] and ion implantation[26,42]), our metal matrix−metal nanoparticle composite formation technique enables excellent control over particle size, shape, and composition. By separating the steps of nanoparticle synthesis and nanocomposite formation, we have enabled independent quality control over nanoparticle morphology and facile control over nanoparticle volume fraction. This concept of separating nanoparticle synthesis and nanocomposite formation has been previously demonstrated to produce nanocomposites with organic matrices,[43−45] oxide matrices,[46,47] and semiconductor matrices.[48−50] Herein, we have applied this concept to metal matrix nanocomposites. We do note that identifying appropriate metal precursors is not trivial because many precursors decompose into metal−oxide instead of metal. This was another reason for our choice of a silver matrix; in addition to its favorable phase behavior with bismuth and its very high thermal conductivity, it is energetically favorable to form silver over silver oxide due to silver's high reduction potential. By judicious selection of solvents, nanoparticles, and metal precursors, we believe this approach can be generalized to other metal nanocomposite chemical compositions. Soluble metal precursors that decompose into copper,[51,52] silver,[53,54] gold,[55] palladium,[56] cobalt,[57] and rhodium[57] have been identified in the literature.

Nanocomposite Melting Temperature and Thermal Energy Storage Density. To investigate the melting characteristics of our Ag matrix−Bi nanoparticle composites, differential scanning calorimetry (DSC) measurements were performed. A representative heating and cooling cycle of a nanocomposite containing 13.2 nm Bi nanoparticles is shown in Figure 4a. One endothermic valley was observed at 246 °C during heating, and we attribute this to nanoparticle melting. In accordance with size-dependent melting, this melting occurs well below the melting temperature of bulk Bi, 271 °C. During cooling, three exothermic peaks were observed. The first peak was broad and appeared around 224 °C, whereas the second and third peak appeared around 137 and 93 °C, respectively. We attribute these peaks to three separate nanoparticle freezing events because the total energy released is equivalent to the energy absorbed during nanoparticle melting; these data suggest that three different nucleation mechanisms are present within our nanocomposite. The Bi nanoparticles also exhibit a significant amount of supercooling, which could likely be mitigated *via* surface chemistry modification on the nanoparticles.[58] The melting and freezing assignments in our nanocomposite were corroborated by a control DSC measurement on silver prepared *via* silver benzoate thermal decomposition. No discernible features in the control measurement are observed throughout

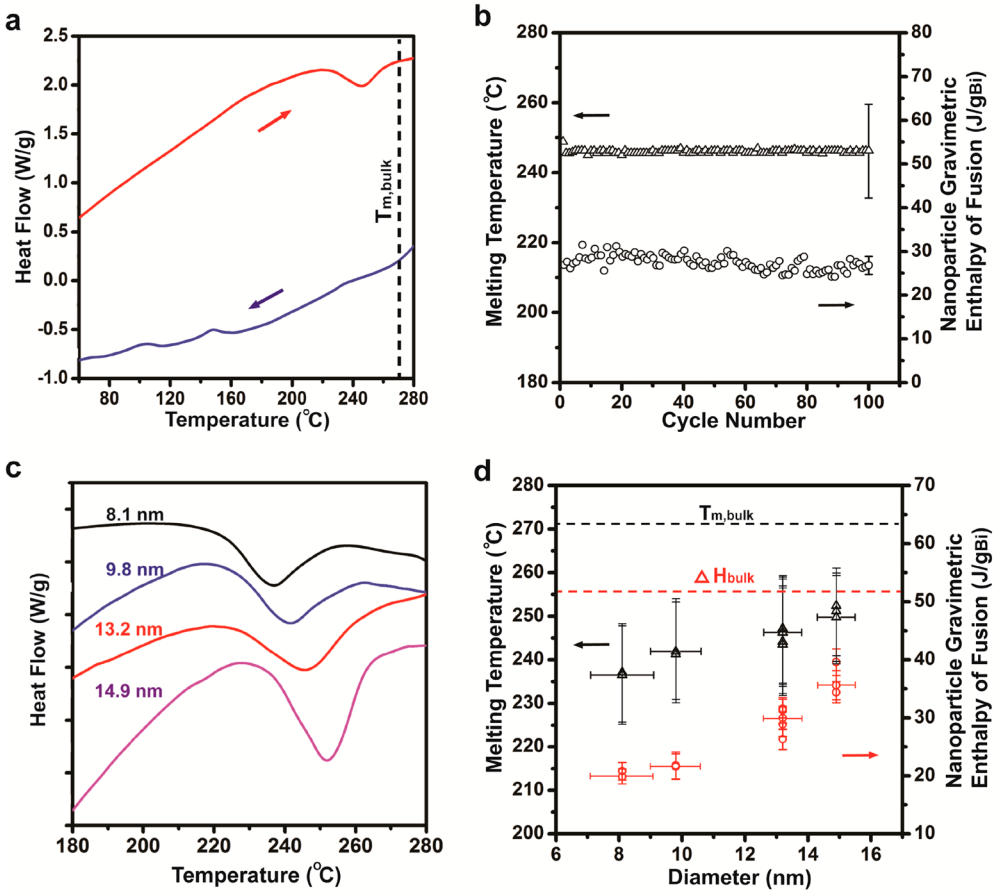

Figure 4. (a) Heating and cooling DSC cycle for a composite with Bi nanoparticles (NPs) of 13.2 nm diameter. (b) Melting characteristics of a composite with 13.2 nm Bi nanoparticles throughout 100 thermal cycles. (c) Endothermic melting valley during DSC measurements on composites with different Bi nanoparticle diameters. For clarity, the data in (c) have been offset along the vertical axis; each tick mark represents 0.2 W/g. (d) Size-dependent melting temperature (triangles) and enthalpy of fusion (circles) for the Bi nanoparticles. All nanocomposites in (a)−(d) have a similar nanoparticle volume fraction of approximately 0.20−0.25. We note that the large error bars for melting temperature in (b) and (d) arise from our use of the endothermic valley's full width half-maximum for the measurement uncertainty. We use the location of the endothermic valley minimum as the melting temperature, and these variations were insignificant as seen in part (b).

the entire temperature range (Figure S2, Supporting Information). In addition to facilitating fast thermal transport, the composite's Ag matrix is also intended to function as a nanoparticle isolation barrier that prevents nanoparticle coalescence during melt−freeze cycles. To examine the matrix's effectiveness, we subjected a composite to 100 melt−freeze cycles. As shown in Figure 4b, no notable changes in melting temperature or enthalpy of fusion were observed throughout the cycles. Note that in Figure 4 we have used the location of the endothermic valley minimum and full width half-maximum for the melting temperature and melting temperature uncertainty, respectively.

One benefit of employing nanoparticles as PCM is that the melting temperature can be tuned *via* particle diameter. This design variable provides additional flexibility when engineering the working temperature of a PCM. To demonstrate this capability, we prepared 12 composites containing 8.1 ± 1.0, 9.8 ± 0.8, 13.2 ± 0.6, and 14.9 ± 0.6 nm Bi nanoparticles. As the nanoparticle diameter varied from 8.1−14.9 nm, the melting temperature varied from 236 to 252 °C (Figure 4c,d). We also observe a size-dependent enthalpy of fusion that accompanies the size-dependent melting temperature; the nanoparticle enthalpy of fusion varied from 20.1−37.6 J/g_{Bi} over our range of nanoparticle diameters (Figure 4c,d). Our prior work on Bi nanoparticles in polymer matrices showed different ranges of melting temperature and enthalpy of fusion in similarly sized nanoparticles (218−240 °C and 12.9−42.1 J/g_{Bi}).[45] This indicates that the melting temperature and enthalpy of fusion of nanoparticles is a function of both size and surrounding environment. Past observations of size-dependent enthalpy of fusion required the use of sophisticated nanocalorimetry techniques.[59] It is notable that we are able to extract size-dependent enthalpies of fusion using widely available standard benchtop DSC measurements. This is possible because our nanocomposite formation technique yields large sample sizes of monodisperse nanoparticles, accurate Bi volume fraction control, and protection against nanoparticle coalescence. We now

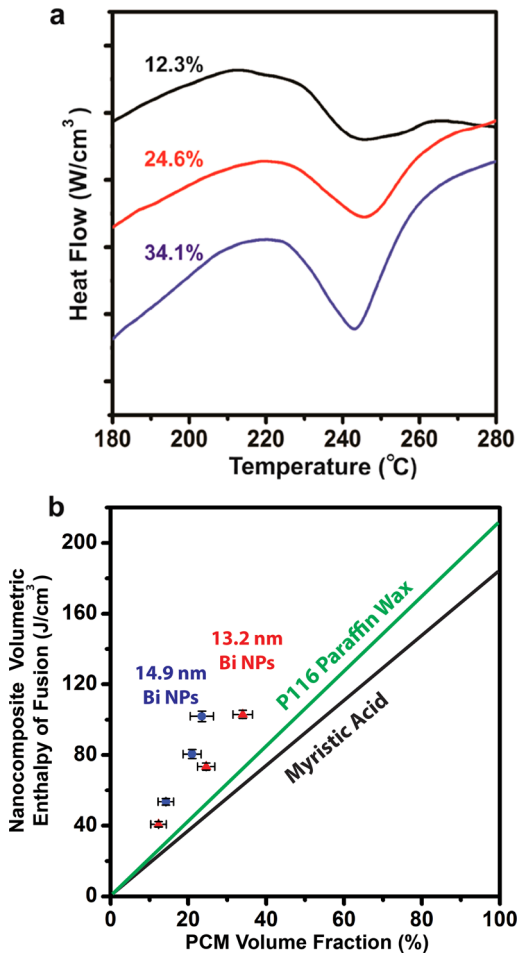

Figure 5. (a) Endothermic melting valley during DSC measurements on composites with 13.2 nm diameter Bi nanoparticles and varying Bi volume fraction. For clarity, the data in (a) have been offset along the vertical axis; each tick mark represents 0.5 W/cm^3. (b) Effective volumetric energy density for composites containing 13.2 and 14.9 nm Bi nanoparticles with varying Bi nanoparticle volume fractions. For comparison, two common organic phase change materials, P116 paraffin wax and myristic acid, are also shown.

note that this paper discusses two different types of enthalpy of fusion. The first one is the gravimetric enthalpy of fusion of the nanoparticle component in the composite, which is the enthalpy of fusion discussed above and in Figure 4. In the following discussion and Figure 5, we focus on the nanocomposite's effective volumetric enthalpy of fusion. We note that we use nanocomposite mass to deduce nanocomposite volume, and hence, the volumetric enthalpy of fusions below do not account for porosity effects.

The thermal energy storage density of the composite can be controlled independent of melting temperature by varying the nanoparticle volume fraction. As shown in Figure 5a, the composite exhibits an increase in volumetric enthalpy of fusion as the volume fraction of Bi nanoparticles is increased. This enables a simple two-step process for PCM design. First, the nanoparticle size is chosen to yield the desired melting temperature. Second, the Bi content is varied to yield the desired composite volumetric enthalpy of fusion.

We successfully increased the Bi nanoparticle volume fraction to ~34% without observing detrimental effects on melting temperature (*i.e.*, nanoparticle coalescence during melt-freeze cycling), which indicates that the Ag matrix effectively protects to this level of nanoparticle loading (Figure 5a). The Bi volume fraction in the nanocomposite was determined by using the relative concentrations of the bismuth nanoparticle and silver benzoate solutions. Since the Bi nanoparticle solution contains both the nanoparticles and surface ligands, we used a procedure described in our prior work[45] to determine the nanoparticle solution's true Bi content. Our nanocomposites achieve a ~ 50−100% enhancement in volumetric energy density relative to composites with an equivalent volume fraction of typical organic PCMs (Figure 5b).[60,61] However, due to nanoparticle coalescence at high nanoparticle volume fractions, the maximum PCM volume fraction in our composites is lower than that achievable with organic PCM composites.

Nanocomposite Thermal Transport. Another objective of this nanocomposite design is to facilitate fast thermal charging/discharging. Conventional thermal storage materials such as paraffins, salt hydrates, and inorganic salts have poor thermal conductivities on the order of 10^{-1}−10^{0} W/m-K, which lead to poor thermal charging/discharging rates. In contrast, metals have thermal conductivities ranging from 10^{1} to 10^{2} W/m-K, which suggests our metal nanocomposite should have superior thermal transport performance. To validate this conjecture, we measured the thermal conductivity of our nanocomposites using the Wiedemann−Franz law.[29]

The Wiedemann−Franz law states that the thermal conductivity, k, of metallic materials can be related to the electrical conductivity, σ, *via* the Lorenz number, L, and absolute temperature, T.

$$k = L\sigma T$$

For most metals, the Sommerfeld value for the Lorenz number, L_0, is a reasonable approximation[62,63]

$$L_0 = \frac{\pi^2 k_B^2}{3e^2} = 2.44 \times 10^{-8}\ \mathrm{W\,\Omega\,K^{-2}}$$

where k_B and e are the Boltzmann constant and elementary charge, respectively. In general, both electrons and phonons conduct heat in solids, and so it should be noted that thermal conductivity measurements obtained using the Wiedemann−Franz law approach only contain electron contributions.[29,64] However, since the phonon contribution to thermal conductivity in metals is negligible, this approach effectively measures the total thermal conductivity in our nanocomposites.[64] We prepared thin film nanocomposite samples by spin-coating and then measured their corresponding electrical conductivity using the

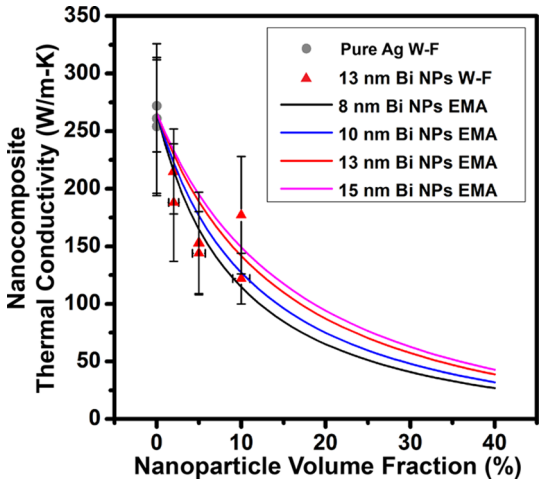

Figure 6. Nanocomposite thermal conductivity measurements using the Wiedemann–Franz (W–F) law and thermal conductivity calculations using the modified effective medium approximation (EMA) for varying nanoparticle (NP) diameter and volume fraction.

Van der Pauw method. The thermal conductivity was then obtained using the Sommerfeld value for the Lorenz number in the Wiedemann–Franz law.

We measured the thermal conductivity of nanocomposites containing 13 nm Bi nanoparticles with volume fractions ranging from 0 to 10% (Figure 6). The nanocomposite thermal conductivity varied from 270 ± 61 to 128 ± 23 W/m-K over this range, and larger Bi nanoparticle volume fractions resulted in lower thermal conductivities. Notably, these thermal conductivity values are significantly greater than typical thermal storage materials by several orders of magnitude. The thermal conductivity of our nanocomposite with 0% Bi nanoparticles corresponds to silver prepared *via* thermal decomposition of silver benzoate and is approximately 40% less than literature values for bulk silver. Given that our Ag samples exhibit porosity and are nanocrystalline with grain sizes on the order of 100 nm (see Figure S3, Supporting Information), this moderate decrease in thermal conductivity is reasonable. The uncertainty in nanocomposite thermal conductivity was dominated by film thickness uncertainty caused by roughness. Samples with Bi nanoparticle fractions greater than 10 vol % were not experimentally measured due to poor film quality. We also note that our use of the Sommerfeld value for the Lorenz number assumes that the nanocomposite's electron gas is degenerate and that the electron mean free path is the same for both electrical conductivity and thermal conductivity.[62,63] Since Lorenz number deviations of up to ~50% from the Sommerfeld value have been reported in the literature,[65,66] our use of this value introduces additional uncertainty. Nonetheless, this uncertainty is relatively small given the several orders of magnitude improvement in thermal conductivity of our nanocomposites.

The nanocomposite thermal conductivity decreases from 215 ± 51 to 128 ± 23 W/m-K as the volume fraction of 13 nm Bi nanoparticles increases from 2 to 10%. This thermal conductivity trend arises due to two different effects. The first effect is that increasing nanoparticle volume fraction decreases the thermal conductivity of the Ag matrix itself. This arises because the nanocomposite's interface density is commensurate with the mean free path of the thermal energy carriers in the Ag phase (*i.e.*, ~33 nm, see the Supporting Information). These interfaces act as scattering sites, which leads to smaller effective mean free paths in the Ag and lower Ag thermal conductivities. The second effect causing this thermal conductivity trend is that the volume fraction of the highly conductive Ag component decreases as the nanoparticle volume increases. It should also be noted that due to the finite thermal interface conductance between the Ag and Bi, the Bi nanoparticles contribute a negligible amount to the overall nanocomposite thermal conductivity. Based on experimental data for similar interfaces,[67,68] we estimate that the thermal interface conductance between the Bi nanoparticles and the Ag matrix is 34 MW/m^2-K (this value is lower than typical metal–metal interface conductances[69] due to the presence of organic ligands at the Bi–Ag interface). For reference purposes, an interface conductance can be converted into an equivalent film thickness by dividing the film's thermal conductivity by its thickness. In the case of our nanocomposite, the interface conductance between the Bi nanoparticles and Ag matrix is equivalent to a 7.9 μm thick Ag film. Consequently, the nanocomposite's thermal conductivity is dominated by the thermal conductivity of the monolithic Ag matrix and smaller Ag matrix volume fractions directly lead to small thermal conductivities.

To further explore the effects of nanoparticle size and volume fraction on the nanocomposite thermal conductivity, we utilize a modified effective medium approximation (EMA) that accounts for nanoscale thermal transport effects. The conventional EMA approach is invalid for nanostructured materials because large interface densities lead to enhanced scattering of thermal energy carriers. This scattering leads to thermal conductivity changes in the nanocomposite as well as the individual nanocomposite constituents themselves. The modified EMA approach suggested by Minnich and Chen[70] addresses this issue by accounting for interface density when estimating the mean free path of thermal energy carriers. Using their modified EMA approach, they obtained good agreement with more sophisticated Monte Carlo calculations on nanocomposite thermal conductivity. Recently, Ong *et al.*[71] successfully applied this approach to fit experimental thermal conductivity data on nanocrystal arrays composed of nanoparticles with structures similar to those of the nanoparticles in our work. Consequently, we believe this modified EMA method

should provide reasonable predictions for the thermal conductivity of our nanocomposites. Note that the original work by Minnich and Chen[70] focused on thermal transport *via* phonons. Since our nanocomposites are metallic, the predominant heat carriers are free electrons instead of phonons and we have adapted our calculations to account for this. We neglect the phonon contribution to thermal conductivity because it is typically 3 orders of magnitude smaller than the electron contribution in metals. Additional calculation details can be found in the Supporting Information.

Figure 6 directly compares our modified EMA calculations with our experimental measurements. Given our measurement uncertainty, these results are in reasonable agreement. These calculations indicate that our nanocomposites with ~35 vol % Bi (*i.e.*, the highest volume fraction for which melting point depression could be maintained) have a thermal conductivity of approximately 33 to 52 W/m-K for nanoparticle diameters from 8 to 15 nm. Changing the Ag−Bi thermal interface conductance and/or the Bi nanoparticle thermal conductivity by several orders of magnitude in the EMA calculations had negligible effects on the nanocomposite thermal conductivity (see the Supporting Information). This supports our previous assertions that the dominant factors causing the nanocomposite thermal conductivity trend for increasing Bi nanoparticle volume fraction are decreases in Ag thermal conductivity and Ag volume fraction. These modified EMA calculations also indicate that smaller Bi nanoparticle diameters lead to smaller nanocomposite thermal conductivities. This can be understood by realizing that for equivalent volume fractions, the Ag−Bi interface density increases as the Bi nanoparticle diameter decreases. This increased interface density causes the effective mean free path in the Ag matrix to decrease and consequently the thermal conductivity of the Ag matrix itself decreases as nanoparticle diameter decreases. Overall, our combined thermal conductivity calculations and modified EMA calculations indicate that our nanocomposite thermal conductivity is on the order of 10^1-10^2 W/m-K, which is several orders of magnitude better than typical thermal storage materials (*e.g.*, $10^{-1} - 10^0$).[4,10] This increased thermal conductivity improves thermal energy storage performance *via* significantly faster thermal charging/discharging times.

CONCLUSION

We have created nanocomposites that consist of phase-change Bi nanoparticles embedded in an Ag matrix. Our nanocomposite formation approach enables excellent control over nanoparticle size, shape, and volume fraction and can likely be generalized to other metal matrix−metal nanoparticle compositions. Using these Ag matrix−Bi nanoparticle composites, we have experimentally demonstrated PCMs with tunable melting temperatures and large thermal energy densities. The Ag matrix preserves the nanocomposite structure during melt−freeze cycles and enables excellent thermal conductivities. Thermal conductivity measurements and modified EMA calculations indicate that our nanocomposite thermal conductivity is on the order of 10^1-10^2 W/m-K, which is several orders of magnitude better than typical thermal storage materials. Overall, this metal matrix−metal nanoparticle composites represents a new paradigm for PCMs that can be used for thermal storage and management applications.

MATERIALS AND METHODS

Materials and Equipment. All reagents and solvents were purchased from Sigma-Aldrich. Sample imaging was done with transmission electron microscopy (TEM, Tecnai F20) and scanning electron microscopy (SEM, Nova 200 NanoLab FEI). The X-ray diffraction was taken on a high-resolution X-ray diffractometer (XRD, PANALYTICAL X'PERT PRO) with CuKα X-ray source operating at 40 kV and 40 mA. The thermogravimetric analysis and differential scanning calorimetry were performed using a TA Instruments Q500 TGA and TA Instruments Q20 DSC. Elemental analysis was carried out by energy dispersive spectroscopy (EDS, EDAX). The masses of nanoparticles and nanocomposites were determined using a Mettler Toledo UMX2 Ultra-Microbalance. Thin-film conductivity measurements were performed with a Keithley 2400 sourcemeter, and film thicknesses were determined by profilometry (Dektak XT stylus profilometer). Unless otherwise indicated, all samples were prepared and stored in an air-free environment. Samples were exposed to air for brief periods when using the above instruments.

Bi Precursor Synthesis. $Bi[N(SiMe_3)_2]_3$ is a metal silylamide and was used as the Bi precursor in this work. This precursor was prepared by reacting $BiCl_3$ and $Li[N(SiMe_3)_2]$ at 0 °C for 2 h.[30] In a typical synthesis, two solutions were prepared in a nitrogen-filled glovebox: (1) 3.34 g of $Li[N(SiMe_3)_2]$ dissolved in 40 mL of diethyl ether and (2) 2.10 g of $BiCl_3$ dissolved in a mixture of 40 mL diethyl ether and 10 mL of tetrahydrofuran (THF). Solution 1 was first added into the flask and cooled to 0 °C with an ice bath. Solution 2 was then added dropwise to the flask and reacted for 2 h. After 2 h, the reaction mixture was a nontransparent yellow color and was then filtered through a PTFE filter (pore size 200 nm). The resulting bright yellow solution was dried under vacuum for 1 h and then redissolved in 15 mL of anhydrous pentane. The solution was again filtered and dried under vacuum for another 2 h. The final product $Bi[N(SiMe_3)_2]_3$ was a yellow powder and stored in a nitrogen-filled glovebox for future use.

Bi Nanoparticle Synthesis. In a typical 13 nm Bi nanoparticle synthesis, 20 g of hexdecylamine (HDA) was loaded into a three-neck flask and degassed before heating to 130 °C. At this temperature, two solutions were injected into the flask with a time interval of 15 s between injections. The first solution was 100 μL of 1 M $Li(Et_3BH)$ in THF, and the second was 0.14 g of $Bi[N(SiMe_3)_2]_3$ and 0.17 g of $Li[N(SiMe_3)_2]$ codissolved in 2 mL of toluene. Fifteen seconds after the second injection, the flask was swiftly removed from the heating mantle and cooled using a water bath. During cooling, 20 mL of toluene was injected into the reaction mixture to prevent the HDA from solidifying. Once the temperature dropped to 40 °C, the flask was disconnected from the Schlenk line and the cleaning process was done in air. The Bi nanoparticles were isolated from the mixture by precipitating with a 1:1 addition of ethanol and centrifuging at

3000 rpm for 5 min. It should be noted that this synthesis yields Bi nanoparticles with surface-bound HDA ligands. We switched these HDA ligands for oleic acid ligands immediately after the first precipitation, which led to improved colloidal nanoparticle solution stability. The Bi nanoparticles were further cleaned three times by precipitating with ethanol and finally suspended in toluene.

Nanocomposite Formation. The nanocomposites were prepared in three steps. First, the Bi nanoparticles were synthesized as described above. The nanoparticles were further cleaned by additional precipitations with ethanol and then dissolved in toluene with a concentration of ~1 mg/mL. A fresh silver precursor solution was prepared by dissolving silver benzoate using pyridine and stirring overnight. The concentration of silver benzoate solution was ~2 mg/mL. Second, an appropriate amount of Bi nanoparticle suspension and silver benzoate solution were combined to yield the desired Bi nanoparticle volume fraction and this combined solution was stirred for an additional 2 h. This combined solution was then filtered through a PTFE filter and drop-cast on appropriate substrates (*e.g.*, DSC pan or TEM silicon nitride window). Finally, the cast film was thermally annealed in two steps: 100 °C for 1 h and then 300 °C for 2 h in a nitrogen atmosphere.

DSC Measurements. All DSC samples were prepared by drop-casting an appropriate amount of Bi nanoparticle−silver benzoate combined solution into an aluminum DSC pan. The sample was then subjected to a two-step thermal anneal in a nitrogen atmosphere as described above. During DSC experiments, all samples were heated and cooled between 0 to 300 °C at a rate of 10 °C/min for at least 15 cycles.

Thermal Conductivity Measurements. The thermal conductivity measurements were carried out by first measuring electrical conductivity using the Van der Pauw method and then converting this electrical conductivity into a thermal conductivity using the Wiedemann−Franz law.[29] Samples for thermal conductivity measurements were prepared on silicon substrates by spin coating 100 μL of solution at 1500 rpm. The film was then heated sequentially at 100 and 350 °C. In some instances, this deposition process was repeated to yield an appropriate film thickness. Final film thicknesses were typically 200−600 nm.

TEM Sample Preparation and Particle Size Determination. All Bi nanoparticle TEM samples were prepared by drop-casting 50 μL of a dilute nanoparticle suspension onto a carbon film supported copper TEM grid. The nanoparticle diameter was determined with ImageJ by analyzing a representative TEM image containing 100−200 Bi nanoparticles. The diameter uncertainties in manuscript represent the standard deviation of the nanoparticle diameters. The nanocomposite TEM samples were prepared by drop-casting a dilute combined solution of Bi nanoparticles and silver benzoate onto a Si_3N_4 window and then annealed as described in the Nanocomposite Formation section above.

Conflict of Interest: The authors declare no competing financial interest.

Supporting Information Available: Additional details on the modified effective medium approximation calculations; figures showing scanning electron microscopy images, energy dispersive X-ray spectroscopy chemical composition maps, DSC data, and modified effective medium approximation results on nanocomposite thermal conductivity. This material is available free of charge *via* the Internet at http://pubs.acs.org.

Acknowledgment. This work was supported by the National Science Foundation through Grant No. CBET-1236656. We gratefully acknowledge the use of facilities within the LeRoy Eyring Center for Solid State Science at Arizona State University. We thank Lenore Dai for use of her thermogravimetric analyzer.

REFERENCES AND NOTES

1. Hyun, D. C.; Levinson, N. S.; Jeong, U.; Xia, Y. Emerging Applications of Phase-Change Materials (PCMs): Teaching an Old Dog New Tricks. *Angew. Chem., Int. Ed.* **2014**, *53*, 3780–3795.
2. Liu, C.; Li, F.; Ma, L. P.; Cheng, H. M. Advanced Materials for Energy Storage. *Adv. Mater.* **2010**, *22*, E28–E62.
3. Sharma, A.; Tyagi, V. V.; Chen, C. R.; Buddhi, D. Review on Thermal Energy Storage with Phase Change Materials and Applications. *Renewable Sustainable Energy Rev.* **2009**, *13*, 318–345.
4. Kenisarin, M.; Mahkamov, K. Solar Energy Storage Using Phase Change Materials. *Renewable Sustainable Energy Rev.* **2007**, *11*, 1913–1965.
5. Pasupathy, A.; Velraj, R.; Seeniraj, R. V. Phase Change Material-Based Building Architecture for Thermal Management in Residential and Commercial Establishments. *Renewable Sustainable Energy Rev.* **2008**, *12*, 39–64.
6. Krishnan, S.; Garimella, S. V. Thermal Management of Transient Power Spikes in Electronics - Phase Change Energy Storage or Copper Heat Sinks? *J. Electron. Packag.* **2004**, *126*, 308–316.
7. Tamme, R.; Bauer, T.; Buschle, J.; Laing, D.; Müller-Steinhagen, H.; Steinmann, W.-D. Latent Heat Storage above 120°C for Applications in the Industrial Process Heat Sector and Solar Power Generation. *Int. J. Energy Res.* **2008**, *32*, 264–271.
8. Lu, T. J. Thermal Management of High Power Electronics with Phase Change Cooling. *Int. J. Heat Mass Transfer* **2000**, *43*, 2245–2256.
9. Stekli, J.; Irwin, L.; Pitchumani, R. Technical Challenges and Opportunities for Concentrating Solar Power With Thermal Energy Storage. *J. Therm. Sci. Eng. Appl.* **2013**, *5*, 021011–021011.
10. Kenisarin, M. M. High-Temperature Phase Change Materials for Thermal Energy Storage. *Renewable Sustainable Energy Rev.* **2010**, *14*, 955–970.
11. Flueckiger, S.; Yang, Z.; Garimella, S. V. An Integrated Thermal and Mechanical Investigation of Molten-Salt Thermocline Energy Storage. *Appl. Energy* **2011**, *88*, 2098–2105.
12. Ji, H.; Sellan, D. P.; Pettes, M. T.; Kong, X.; Ji, J.; Shi, L.; Ruoff, R. S. Enhanced Thermal Conductivity of Phase Change Materials with Ultrathin-Graphite Foams for Thermal Energy Storage. *Energy Environ. Sci.* **2014**, *7*, 1185–1192.
13. Schiffres, S. N.; Harish, S.; Maruyama, S.; Shiomi, J.; Malen, J. A. Tunable Electrical and Thermal Transport in Ice-Templated Multi layer Graphene Nanocomposites through Freezing Rate Control. *ACS Nano* **2013**, *7*, 11183–11189.
14. Zalba, B.; Marin, J. M.; Cabeza, L. F.; Mehling, H. Review on Thermal Energy Storage with Phase Change: Materials, Heat Transfer Analysis and Applications. *Appl. Therm. Eng.* **2003**, *23*, 251–283.
15. Li, M. A Nano-Graphite/Paraffin Phase Change Material with High Thermal Conductivity. *Appl. Energy* **2013**, *106*, 25–30.
16. Parameshwaran, R.; Jayavel, R.; Kalaiselvam, S. Study on Thermal Properties of Organic Ester Phase-Change Material Embedded with Silver Nanoparticles. *J. Therm. Anal. Calorim.* **2013**, *114*, 845–858.
17. Chen, L.; Zou, R.; Xia, W.; Liu, Z.; Shang, Y.; Zhu, J.; Wang, Y.; Lin, J.; Xia, D.; Cao, A. Electro and Photodriven Phase Change Composites Based on Wax-Infiltrated Carbon Nanotube Sponges. *ACS Nano* **2012**, *6*, 10884–10892.
18. Cui, H. T. Experimental Investigation on the Heat Charging Process by Paraffin Filled with High Porosity Copper Foam. *Appl. Therm. Eng.* **2012**, *39*, 26–28.
19. Lafdi, K.; Mesalhy, O.; Elgafy, A. Graphite Foams Infiltrated with Phase Change Materials as Alternative Materials for Space and Terrestrial Thermal Energy Storage Applications. *Carbon* **2008**, *46*, 159–168.
20. Zhao, C. Y.; Wu, Z. G. Heat Transfer Enhancement of High Temperature Thermal Energy Storage Using Metal Foams and Expanded Graphite. *Sol. Energy Mater. Sol. Cells* **2011**, *95*, 636–643.
21. Pawlow, P. The Dependency of The Melting Point on the Surface Energy of a Solid Body. (Supplement). *Z. Phys. Chem.* **1909**, *65*, 545–548.
22. Buffat, P.; Borel, J. P. Size Effect on Melting Temperature of Gold Particles. *Phys. Rev. A* **1976**, *13*, 2287–2298.

23. Couchman, P. R.; Jesser, W. A. Thermodynamic Theory of Size Dependence of Melting Temperature in Metals. *Nature* **1977**, *269*, 481–483.
24. Liang, L. H.; Li, J. C.; Jiang, Q. Size-Dependent Melting Depression and Lattice Contraction of Bi Nanocrystals. *Phys. B* **2003**, *334*, 49–53.
25. Hu, J.; Hong, Y.; Muratore, C.; Su, M.; Voevodin, A. A. *In-situ* Transmission Electron Microscopy of Solid-Liquid Phase Transition of Silica Encapsulated Bismuth Nanoparticles. *Nanoscale* **2011**, *3*, 3700–3704.
26. Xu, Q.; Sharp, I. D.; Yuan, C. W.; Yi, D. O.; Liao, C. Y.; Glaeser, A. M.; Minor, A. M.; Beeman, J. W.; Ridgway, M. C.; Kluth, P.; *et al.* Large Melting-Point Hysteresis of Ge Nanocrystals Embedded in SiO_2. *Phys. Rev. Lett.* **2006**, *97*, 155701.
27. Tang, C. Y.; Sung, Y. M.; Lee, J. Nonlinear Size-Dependent Melting of the Silica-Encapsulated Silver Nanoparticles. *Appl. Phys. Lett.* **2012**, *100*, 201903.
28. Goldstein, A. N.; Echer, C. M.; Alivisatos, A. P. Melting in Semiconductor Nanocrystals. *Science* **1992**, *256*, 1425–1427.
29. Neil W. Ashcroft, N. D. M *Solid State Physics*; Holt, Rinehart and Winston: New York 1976; p 33−53.
30. Yarema, M.; Kovalenko, M. V.; Hesser, G.; Talapin, D. V.; Heiss, W. Highly Monodisperse Bismuth Nanoparticles and Their Three-Dimensional Superlattices. *J. Am. Chem. Soc.* **2010**, *132*, 15158–15159.
31. Dujardin, E.; Peet, C.; Stubbs, G.; Culver, J. N.; Mann, S. Organization of Metallic Nanoparticles Using Tobacco Mosaic Virus Templates. *Nano Lett.* **2003**, *3*, 413–417.
32. Kumar, A.; Vemula, P. K.; Ajayan, P. M.; John, G. Silver-Nanoparticle-Embedded Antimicrobial Paints Based on Vegetable Oil. *Nat. Mater.* **2008**, *7*, 236–241.
33. Murray, C. B.; Norris, D. J.; Bawendi, M. G. Synthesis and Characterization of Nearly Monodisperse CdE (E = S, Se, Te) Semiconductor Nanocrystallites. *J. Am. Chem. Soc.* **1993**, *115*, 8706–8715.
34. Hanrath, T.; Veldman, D.; Choi, J. J.; Christova, C. G.; Wienk, M. M.; Janssen, R. A. J. PbSe Nanocrystal Network Formation during Pyridine Ligand Displacement. *ACS Appl. Mater. Interfaces* **2009**, *1*, 244–250.
35. *Binary Alloy Phase Diagrams 2.2*; The Materials Information Society: Materials Park, OH, 1996.
36. Gråbaek, L.; Bohr, J.; Johnson, E.; Johansen, A.; Sarholt-Kristensen, L.; Andersen, H. Superheating and Supercooling of Lead Precipitates in Aluminum. *Phys. Rev. Lett.* **1990**, *64*, 934–937.
37. Zhong, J.; Zhang, L. H.; Jin, Z. H.; Sui, M. L.; Lu, K. Superheating of Ag Nanoparticles Embedded in Ni Matrix. *Acta Mater.* **2001**, *49*, 2897–2904.
38. Meitl, M. A.; Dellinger, T. M.; Braun, P. V. Bismuth-Ceramic Nanocomposites with Unusual Thermal Stability *via* High-Energy Ball Milling. *Adv. Funct. Mater.* **2003**, *13*, 795–799.
39. Poudel, B.; Hao, Q.; Ma, Y.; Lan, Y.; Minnich, A.; Yu, B.; Yan, X.; Wang, D.; Muto, A.; Vashaee, D.; *et al.* High-Thermoelectric Performance of Nanostructured Bismuth Antimony Telluride Bulk Alloys. *Science* **2008**, *320*, 634–638.
40. Haro-Poniatowski, E.; Jimenez de Castro, M.; Fernandez Navarro, J. M.; Morhange, J. F.; Ricolleau, C. Melting and Solidification of Bi Nanoparticles in a Germanate Glass. *Nanotechnology* **2007**, *18*, 315703.
41. Mu, J.; Zhu, Z. W.; Zhang, H. F.; Fu, H. M.; Wang, A. M.; Li, H.; Hu, Z. Q. Size Dependent Melting Behaviors of Nanocrystalline in Particles Embedded in Amorphous Matrix. *J. Appl. Phys.* **2012**, *111*, 043515.
42. Sharp, I. D.; Yi, D. O.; Xu, Q.; Liao, C. Y.; Beeman, J. W.; Liliental-Weber, Z.; Yu, K. M.; Zakharov, D. N.; Ager, J. W.; Chrzan, D. C.; *et al.* Mechanism of Stress Relaxation in Ge Nanocrystals Embedded in SiO2. *Appl. Phys. Lett.* **2005**, *86*, 063107.
43. Bieligmeyer, M.; Taheri, S. M.; German, I.; Boisson, C.; Probst, C.; Milius, W.; Altstadt, V.; Breu, J.; Schmidt, H. W.; D'Agosto, F.; *et al.* Completely Miscible Polyethylene Nanocomposites. *J. Am. Chem. Soc.* **2012**, *134*, 18157–18160.
44. Jeon, K.-J.; Moon, H. R.; Ruminski, A. M.; Jiang, B.; Kisielowski, C.; Bardhan, R.; Urban, J. J. Air-Stable Magnesium Nanocomposites Provide Rapid and High-Capacity Hydrogen Storage without Using Heavy-Metal Catalysts. *Nat. Mater.* **2011**, *10*, 286–290.
45. Liu, M.; Wang, R. Y. Phase Change Nanocomposites with Tunable Melting Temperature and Thermal Energy Storage Density. *Nanoscale* **2013**, *5*, 7234–7237.
46. Llordes, A.; Garcia, G.; Gazquez, J.; Milliron, D. J. Tunable Near-Infrared and Visible-Light Transmittance in Nanocrystal-in-Glass Composites. *Nature* **2013**, *500*, 323–326.
47. Choi, H.; Lee, J. P.; Ko, S. J.; Jung, J. W.; Park, H.; Yoo, S.; Park, O.; Jeong, J. R.; Park, S.; Kim, J. Y. Multipositional Silica-Coated Silver Nanoparticles for High-Performance Polymer Solar Cells. *Nano Lett.* **2013**, *13*, 2204–2208.
48. Kovalenko, M. V.; Scheele, M.; Talapin, D. V. Colloidal Nanocrystals with Molecular Metal Chalcogenide Surface Ligands. *Science* **2009**, *324*, 1417–1420.
49. Tangirala, R.; Baker, J. L.; Alivisatos, A. P.; Milliron, D. J. Modular Inorganic Nanocomposites by Conversion of Nanocrystal Superlattices. *Angew. Chem., Int. Ed.* **2010**, *49*, 2878–2882.
50. Kovalenko, M. V.; Spokoyny, B.; Lee, J.-S.; Scheele, M.; Weber, A.; Perera, S.; Landry, D.; Talapin, D. V. Semiconductor Nanocrystals Functionalized with Antimony Telluride Zintl Ions for Nanostructured Thermoelectrics. *J. Am. Chem. Soc.* **2010**, *132*, 6686–6695.
51. Galwey, A. K.; Jamieson, D.; Brown, M. E. Thermal Decomposition of Three Crystalline Modifications of Anhydrous Copper(II) Formate. *J. Phys. Chem.* **1974**, *78*, 2664–2670.
52. Gupta, A.; Jagannathan, R. Laser Writing of Copper Lines from Metalorganic Films. *Appl. Phys. Lett.* **1987**, *51*, 2254–2256.
53. Fields, E. K.; Meyerson, S. Thermal and Photochemical Decomposition of Silver Carboxylates. *J. Org. Chem.* **1976**, *41*, 916–920.
54. Logvinenko, V.; Polunina, O.; Mikhailov, Y.; Mikhailov, K.; Bokhonov, B. Study of Thermal Decomposition of Silver Acetate. *J. Therm. Anal. Calorim.* **2007**, *90*, 813–816.
55. Bessonov, A. A.; Morozova, N. B.; Semyannikov, P. P.; Trubin, S. V.; Gelfond, N. V.; Igumenov, I. K. Thermal Behaviour of Dimethylgold(III) Carboxylates. *J. Therm. Anal. Calorim.* **2008**, *92*, 751–755.
56. Gallagher, P. K.; Gross, M. E. The Thermal Decomposition of Palladium Acetate. *J. Therm. Anal.* **1986**, *31*, 1231–1241.
57. Fillman, L. M.; Tang, S. C. Thermal Decomposition of Metal-Carbonyls - a Thermogravimetry Mass-Spectrometry Study. *Thermochim. Acta* **1984**, *75*, 71–84.
58. Hong, Y.; Wu, W.; Hu, J.; Zhang, M.; Voevodin, A. A.; Chow, L.; Su, M. Controlling Supercooling of Encapsulated Phase Change Nanoparticles for Enhanced Heat Transfer. *Chem. Phys. Lett.* **2011**, *504*, 180–184.
59. Lai, S. L.; Guo, J. Y.; Petrova, V.; Ramanath, G.; Allen, L. H. Size-Dependent Melting Properties of Small Tin Particles: Nanocalorimetric Measurements. *Phys. Rev. Lett.* **1996**, *77*, 99–102.
60. Himran, S.; Suwono, A.; Mansoori, G. A. Characterization of Alkanes and Paraffin Waxes for Application as Phase-Change Energy Storage Medium. *Energy Sources* **1994**, *16*, 117–128.
61. Hasan, A.; Sayigh, A. A. Some Fatty Acids as Phase-Change Thermal Energy Storage Materials. *Renewable Energy* **1994**, *4*, 69–76.
62. Kumar, G. S.; Prasad, G.; Pohl, R. O. Experimental Determinations of the Lorenz Number. *J. Mater. Sci.* **1993**, *28*, 4261–4272.
63. Sommerfeld, A. The Theory of Electrons of Metals. *Naturwissenschaften* **1928**, *16*, 374–381.
64. Chen, G. *Nanoscale Energy Transport and Conversion: A Parallel Treatment of Electrons, Molecules, Phonons, and Photons*; Oxford University Press: New York, 2005; pp 249−253.
65. Yang, H.; Bahk, J.-H.; Day, T.; Mohammed, A. M. S.; Min, B.; Snyder, G. J.; Shakouri, A.; Wu, Y. Composition Modulation of Ag2Te Nanowires for Tunable Electrical and Thermal Properties. *Nano Lett.* **2014**, *14*, 5398–5404.
66. Zhao, L.-D.; Lo, S.-H.; He, J.; Li, H.; Biswas, K.; Androulakis, J.; Wu, C.-I.; Hogan, T. P.; Chung, D.-Y.; Dravid, V. P.; *et al.*

High Performance Thermoelectrics from Earth-Abundant Materials: Enhanced Figure of Merit in PbS by Second Phase Nanostructures. *J. Am. Chem. Soc.* **2011**, *133*, 20476–20487.
67. Losego, M. D.; Grady, M. E.; Sottos, N. R.; Cahill, D. G.; Braun, P. V. Effects of Chemical Bonding on Heat Transport across Interfaces. *Nat. Mater.* **2012**, *11*, 502–506.
68. Wang, R. Y.; Segalman, R. A.; Majumdar, A. Room Temperature Thermal Conductance of Alkanedithiol Self-Assembled Monolayers. *Appl. Phys. Lett.* **2006**, *89*, 173113.
69. Gundrum, B. C.; Cahill, D. G.; Averback, R. S. Thermal Conductance of Metal-Metal Interfaces. *Phys. Rev. B* **2005**, *72*, 245426.
70. Minnich, A.; Chen, G. Modified Effective Medium Formulation for the Thermal Conductivity of Nanocomposites. *Appl. Phys. Lett.* **2007**, *91*, 073105.
71. Ong, W.-L.; Rupich, S. M.; Talapin, D. V.; McGaughey, A. J. H.; Malen, J. A. Surface Chemistry Mediates Thermal Transport in Three-Dimensional Nanocrystal Arrays. *Nat. Mater.* **2013**, *12*, 410–415.